Materials Advances

ROYAL SOCIETY OF CHEMISTRY

PAPER

View Article Online
View Journal | View Issue

Cite this: *Mater. Adv.*, 2023, 4, 6244

Cobalt oxide decked with inorganic-sulfur containing vanadium oxide for chromium(VI) reduction and UV-light-assisted methyl orange degradation†

Sayanika Saikia,[a] Manoshi Saikia,[a] Salma A. Khanam,[a] Seonghwan Lee,[b] Young-Bin Park,[b] Lakshi Saikia,[c] Gautam Gogoi[a] and Kusum K. Bania *[a]

Cobalt oxide (CoO_x) derived from a zeolitic imidazolate framework (ZIF) was modified with sulfur-doped vanadium oxide (VO_x) using an impregnation method. The presence of inorganic sulfur in the mixed metal oxide matrix was confirmed through various physicochemical and spectroscopic techniques. The hybrid material designated as CoO_x–S–VO_x was applied as a catalyst for rapid reduction of toxic chromium, Cr(VI), in the presence of sodium borohydride, $NaBH_4$. CoO_x–S–VO_x + $NaBH_4$ (1 mmol) reduced Cr(VI) to Cr(III) within three minutes (3 min). The same catalyst possessing a band gap of ~3.14 eV served as an effective photocatalyst for the degradation of methyl orange (MO) dye on irradiating with UV-light. The optimization of different parameters indicated that the degradation of photocatalytic dye proceeded very efficiently within 15 min with a total mineralization of 80.06%. The dye degradation experiments carried out under both light and dark phase conditions truly signified the impact of light irradiation on MO degradation. Mott–Schottky analysis and ultraviolet photoelectron spectroscopy (UPS) were performed to calculate the band edge positions of the material. Both the aforementioned analyses predicted that the hybrid catalyst possessed a perfect band structure that could provide high activity to the material. The mechanistic study of the dye degradation process suggested that the MO decomposition was mostly caused by free radicals. The presence of sulfur was considered to play an active role in enhancing the dye degradation process by reducing the electron–hole recombination rate. The catalyst was recyclable for ten consecutive cycles without any significant loss in catalytic activity.

Received 30th August 2023,
Accepted 17th October 2023

DOI: 10.1039/d3ma00625e

rsc.li/materials-advances

1. Introduction

The gradual increase of industrial areas and the worldwide population boom along with the release of toxic metals or organic pollutants from various industries are causing an adverse impact on the aquatic life cycle.[1,2] The contamination of water bodies with toxic metals and coloured organic molecules is posing a threat to human beings.[3] Out of the many toxic metals, chromium (Cr) mostly used in dye and painting industries is considered to be highly toxic, when present in Cr(VI) form.[4] Depending on the pH of ground water the hexavalent Cr remains as chromate (CrO_4^{2-}) at pH > 6.5 and as $HCrO_4^-$ when pH < 6.5.[5–7] Studies on the toxicity of Cr(VI) have revealed that it can possibly become a health hazard by affecting the respiratory systems of living organisms. Moreover, its severity can affect other human organs such as kidneys and the liver and it also has the potential to cause major genetic disorder.[8] Considering the life threatening impact of Cr(VI), stringent regulations have been imposed by the environmental protection agency (EPA). The EPA has further restricted the standard

[a] *Department of Chemical Sciences, Tezpur University, Assam, 784028, India. E-mail: kusum@tezu.ernet.in, bania.kusum8@gmail.com*
[b] *Department of Mechanical Engineering, Ulsan National Institute of Science and Technology, UNIST-gil 50, Ulju-gun, Ulsan 44919, Republic of Korea*
[c] *Materials Science and Technology Division (MSTD), CSIR-North East Institute of Science and Technology, Jorhat 785006, Assam, India*

† Electronic supplementary information (ESI) available: The supporting information includes data related to physical measurements, DRS and Tauc's plot for S–VO_x and CoO_x, XPS analysis of C(1s) for CoO_x–S–VO_x, EPR, TGA spectra, STEM-HAADF-EDX mapping of the CoO_x–S–VO_x material in different regions, UV spectra and bar diagrams illustrating Cr(VI) reduction efficiency for different Cr(VI) solution concentrations using CoO_x–S–VO_x as well as Cr(VI) reduction efficiency with S–VO_x and CoO_x materials. The information also includes data related to CV plots for Cr(VI) reduction, the efficiency of the catalyst for MO degradation under different conditions, its efficiency in comparison with S–VO_x and CoO_x materials, UV spectra and bar diagrams showing MO degradation for different MO solution concentrations, point of zero charge (PZC) determination and effect of pH on MO degradation using CoO_x–S–VO_x, PL spectra at different excitation wavelengths, UPS spectra, photocatalytic degradation mechanism using an electron scavenger ($AgNO_3$), a hole scavenger (KI), an $OH^•$ scavenger (isopropanol) and an $O_2^{-•}$ scavenger (ascorbic acid), and bar diagram, PXRD spectra, SEM and TEM images for the recyclability test of CoO_x–S–VO_x. See DOI: https://doi.org/10.1039/d3ma00625e

limit of Cr(VI) at 0.1 ppm.[9] In contrast to Cr(VI), its low valent form *i.e.* Cr(III) is less toxic and is necessary for diabetic regulation and is therefore considered as an essential element. Cr(III) can remain as $Cr(OH)_3$ or Cr_2O_3 in water, so they are measured to be less carcinogenic apart from causing some skin rashes when used in excess.[10] Since Cr(III) doesn't have any considerable negative impact on human health and the aquatic life, a substantial amount of previously published research work has been dedicated towards the reduction of poisonous Cr(VI) to non-poisonous Cr(III). Different chemical and photochemical processes have been developed for the reduction of Cr(VI) and accordingly different types of materials and catalysts have been synthesized.[11–17] The reduction processes employ reducing agents like sodium borohydride ($NaBH_4$) and ascorbic acid which are considered to be effective in the presence of suitable materials for the conversion of Cr(VI) to Cr(III).[18–21] As far as the materials are concerned, sulfur-containing transition metals or the metal chalcogenides have shown some promising activity in the removal of Cr(VI).[22–26] Our group has also reported a silver–sulfur–oxido–vanadium cluster for such a reduction process within a very short period of time with $NaBH_4$ as a reducing agent.[27] It is pertinent to mention that sulfur is a familiar insulator, but very recently, the viability and applicability of sulfur in the field of catalysis and photocatalysis have been explored. Compared to many non-metals, sulfur is non-toxic and inexpensive, and hence can be easily handled. However, the scopes of application of sulfur as a single element are lacking and narrow in the field of catalysis. But the advancement of new techniques such as surface modification, nanoscaling, heterojunction creation, doping *etc.* paved a new direction in the utilization of elemental sulfur in the synthesis of effective photoctalysts. It has been reported that the introduction of sulfur or modification of metal oxide with sulfur can bring significant changes by creating some defect sites.[28] The introduction of sulfur in many photocatalysts is found to alter the band gap and enhance the photocatalytic activity of such materials. In this regard the earlier works of Liu *et al.* demonstrated the ability of sulfur crystals of cyclooctasulfur (S_8) to act as a visible-light-active elemental photocatalyst.[29] Furthermore, Jiang *et al.* developed a sulfur-doped g-C_3N_4/g-C_3N_4 heterostructure for the photocatalytic hydrogen evolution reaction with greater stability and reactivity.[30] Similarly, another study conducted by Lu *et al.* synthesized a heterostructure of elemental sulfur supported on ultrathin titanic acid nanosheets in order to improve light and CO_2 adsorption.[31] So, finding the benefits of heterojunctions researchers are driven towards the design of newer photocatalysts or materials for sustainable development.[32–34]

Other than Cr(VI), the coloured dye molecules that are mostly released from textile industries are also harmful for the aquatic life and passively for human beings as well.[35,36] The most challenging part is the decomposition of such coloured dye molecules to CO_2 and H_2O. There are many approaches or chemical treatment techniques by which such toxic dye molecules can be removed from water.[37–42] The photocatalytic decomposition of such dye molecules absorbing the solar energy is considered to be a green and clean process.[43–45] But finding a suitable photocatalyst that can decompose dyes like methyl orange (MO) completely to CO_2 and H_2O is still under study and hence researchers are trying to develop a different low cost photocatalyst that can harvest the solar light and can perform the photodecomposition of dye molecules.

While considering the photocatalyst, the band gap as well as the pH under examination is considered as vital factors in improvising its photocatalytic performance.[46–48] The literature report suggested that by doping metal oxides with sulfur with lower electronegativity than oxygen, polarized d-orbitals with a lone pair of electrons can modulate or alter the photoactivity of metal oxide by changing its band gap as well as the pH.[28] Therefore, looking into the negative impact of Cr(VI) ions and MO dye on our environment, mostly on water and indirectly on human health, herein we have developed a new material by conjugating CoO_x with sulfur containing VO_x that showed excellent activity for the conversion of Cr(VI) to Cr(III). The same material also appeared as a suitable photocatalyst for the photodecomposition of MO. So far, the maximum reported results are mostly concerned with the preparation of one material for one electron transfer process, but the development of one material for two different chemical/photochemical processes will be always advantageous from both economic and synthesis aspects.

2. Experimental section

2.1. Materials

Cobalt(II) chloride hexahydrate ($CoCl_2{\cdot}6H_2O$), ammonium metavanadate (NH_4VO_3) and methyl orange (MO) dye were purchased from Sisco Research Laboratory (SRL). Sodium sulphide flakes nonahydrate ($Na_2S{\cdot}9H_2O$), glacial acetic acid (CH_3COOH), hydrochloric acid (HCl), sulphuric acid (H_2SO_4) (95.0–98%), and nitric acid (HNO_3) were received from E-Merck. Mohr's salt [$Fe(NH_4)_2(SO_4)_2{\cdot}6H_2O$], potassium nitrate ($KNO_3$), and potassium dichromate ($K_2Cr_2O_7$) were procured from HiMedia. Sodium hydroxide (NaOH), orthophosphoric acid (H_3PO_4) potassium iodide (KI), imidazole ($C_3H_4N_2$), silver nitrate ($AgNO_3$), isopropanol and ascorbic acid were received from E-Merck. All the HPLC grade solvents were received from Sigma-Aldrich.

2.2. Synthesis of sulfur containing vanadium oxide, VO_x (S–VO_x)

The synthesis of sulfur-containing vanadium oxide designated as S–VO_x is depicted schematically in Scheme 1a. For the synthesis of sulfur-containing vanadium oxide (S–VO_x), a 0.1 M solution of NH_4VO_3 was prepared dissolving 1.17 g of NH_4VO_3 in 100 mL of distilled water. The solution was made acidic by adding a few drops of glacial acetic acid and stirred for about 30 min at room temperature. To this solution, 0.1 M (2.40 g in 100 mL of distilled water) of sodium sulfide ($Na_2S.9H_2O$) solution was given slowly and constantly stirred for 2 h at 60 °C. The black material produced during the course was repeatedly rinsed with water and finally dried in an oven at 60 °C.

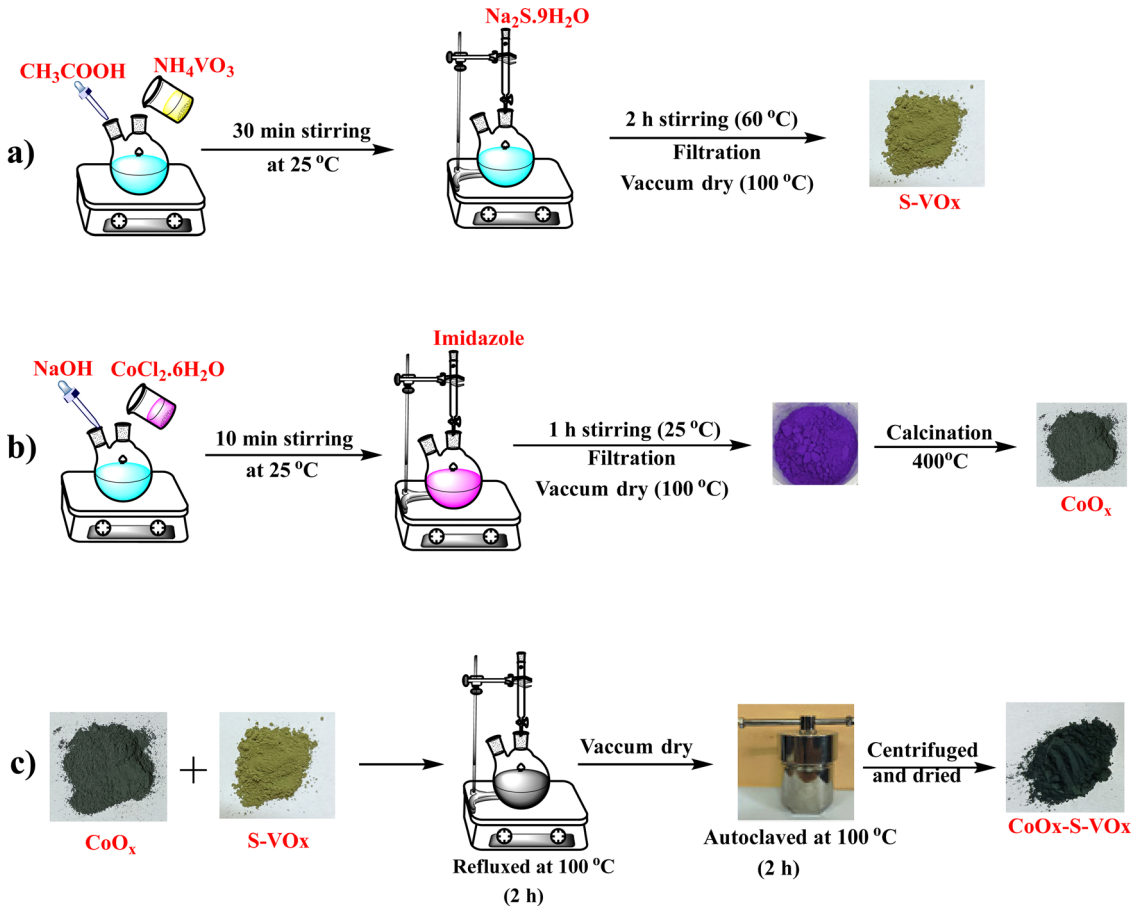

Scheme 1 Schematic representation of the preparation of the CoO_x–S–VO_x catalyst.

2.3. Synthesis of cobalt oxide (CoO_x)

A solution of NaOH (0.1 M) was added to a round bottom flask containing 25 mL of $CoCl_2.6H_2O$ solution (0.1 M). The solution was stirred while maintaining a pH of ~12. To this solution, about 25 mL of 1 M imidazole was added under constant stirring for about 1 h at 60 °C. The violet precipitate obtained was filtered and washed repeatedly with water and ethanol. The oven-dried sample was calcined at 400 °C for about 4 h. The synthesis is depicted in Scheme 1b.

2.4. Preparation of CoO_x–S–VO_x

CoO_x–S–VO_x was synthesized using a hydrothermal method by combining S–VO_x and CoO_x as shown in Scheme 1c. For this, an equal amount (50 mg each) of S–VO_x and CoO_x was mixed in a round bottom flask in water and refluxed for 2 h at 100 °C. The material was further autoclaved for 2 h at 100 °C. After centrifugation, a black material was obtained, which was subsequently dried to get CoO_x–S–VO_x. The overall synthesis process is shown in Scheme 1.

2.5. Preparation of Co_3O_4–V_2O_5

The Co_3O_4–V_2O_5 material prepared previously by our group was used for the comparative study.[49]

2.6. Procedure for Cr(VI) reduction

A 50 mL prepared solution of $K_2Cr_2O_7$ (50 ppm) was taken in a beaker. 10 mg of the CoO_x–S–VO_x catalyst and 1 mmol $NaBH_4$ were added to the above dichromate solution under vigorous stirring conditions. A specific volume of an aliquot was taken out at a specific time interval, centrifuged, and the supernatant was analyzed using UV-Vis spectroscopy. Two UV visible peaks at around 259 and 357 nm were observed for the normal $K_2Cr_2O_7$ solution. However, the peaks were slightly shifted to 271 and 372 nm upon the addition of $NaBH_4$. The disappearance of the peak positions at 271 and 372 nm and the change in solution colour from yellow to colourless were thoroughly examined. It was found that the two UV peaks disappeared within 3 min after adding 10 mg of catalyst followed by 1 mmol $NaBH_4$. The following equation was used to compute the percentage of reduction of Cr(VI).[50,51]

$$\%\text{Reduction} = \frac{(C_o - C_t)}{C_o} \times 100 \quad (1)$$

where C_o = concentration at $t = 0$, C_t = concentration at time t.

2.7. Dye degradation study

The decomposition of MO dye was studied under three different conditions: (i) in a normal laboratory environment without

any external light stimuli, (ii) under the influence of artificial UV-light (λ = 254 nm) using a medium pressure mercury lamp (450 W) and (iii) under dark conditions. For all the cases, 15 mg of our synthesized catalyst CoO_x–S–VO_x in 20 mL of 10^{-6} M MO dye solution in water was taken and the reaction was allowed to proceed for 15 min. The artificial photocatalytic reaction was performed in a photoreactor as mentioned in our previous study.[49]

3. Results and discussion

The X-ray diffraction analysis (XRD) patterns of CoO_x (blue), S–VO_x (red) and CoO_x–S–VO_x(black) are shown in Fig. 1a. The presence of crystalline peak characteristics of Co_3O_4 (JCPDS-00-009-0418), CoO(JCPDS-00-001-1227), V_2O_5(JCPDS-00-003-0207), V_3O_7(JCPDS-00-020-1378) and inorganic sulfur(JCPDS-00-002-0324) in the material confirmed the formation of CoO_x–S–VO_x. FTIR spectra of the materials, S–VO_x(blue), CoO_x(black), and CoO_x–S–VO_x (red) are shown in Fig. 1b. FTIR analysis also confirmed the formation of CoO_x–S–VO_x species. The two bands at 577.4 cm^{-1} and 665.6 cm^{-1} resulting from Co^{+2}–O vibration and Co^{+3}–O vibration of tetrahedral and octahedral sites, respectively, of the Co_3O_4 lattice established the formation of Co_3O_4.[52] The peaks at 1021.4 cm^{-1} and 975.8 cm^{-1} associated with the V = O band and the peak at 826.6 cm^{-1} associated with the V–$(O)_3$ vibrational band of VO_x.[53] The Raman spectra of the materials S–VO_x (blue), CoO_x (black) and CoO_x–S–VO_x (red) are shown in Fig. 1c. The Raman spectra of S–VO_x showed a vibrational band at ~216 cm^{-1} corresponding to inorganic sulfur (S_8). The breathing mode of the V_2O_4 cage was found at ~353 cm^{-1}, while the A_g mode of β-V_2O_5 appeared at ~434 cm^{-1} and ~467 cm^{-1}. The peak at ~152 cm^{-1} was for α-V_2O_5.[54–56] The peaks at ~550 cm^{-1} and ~812 cm^{-1} represented the S–S stretching vibration and terminal V–O bonds, respectively (Fig. 1c (black)).[56,57] Similarly, in the CoO_x material, Raman shifts were noticed at ~187 cm^{-1}, ~466 cm^{-1}, ~510cm^{-1}, ~608 cm^{-1},and ~665 cm^{-1}, confirming the formation of Co_3O_4 (Fig. 1c (red)). Out of which peaks at 187, 510 and 608 cm^{-1} were for F_{2g} symmetry, the peak at 466 cm^{-1} was assigned to E_g symmetry and the peak at 665 cm^{-1} was for A_{1g} symmetry.[58] In the CoO_x–S–VO_x material, the Raman bands at ~216 cm^{-1} were for S_8 and the signals at ~152 cm^{-1}, ~434 cm^{-1}, and ~468 cm^{-1} were for V_2O_5 and bands at ~685 were for Co_3O_4 (Fig. 1c (blue)). The slight shifting of the signals indicated the well mixing of S–VO_x with CoO_x. The presence of the signals for VO_x and CoO_x in the composite material CoO_x–S–VO_x clearly indicated the formation of S_8-containing mixed metal oxide of vanadium and

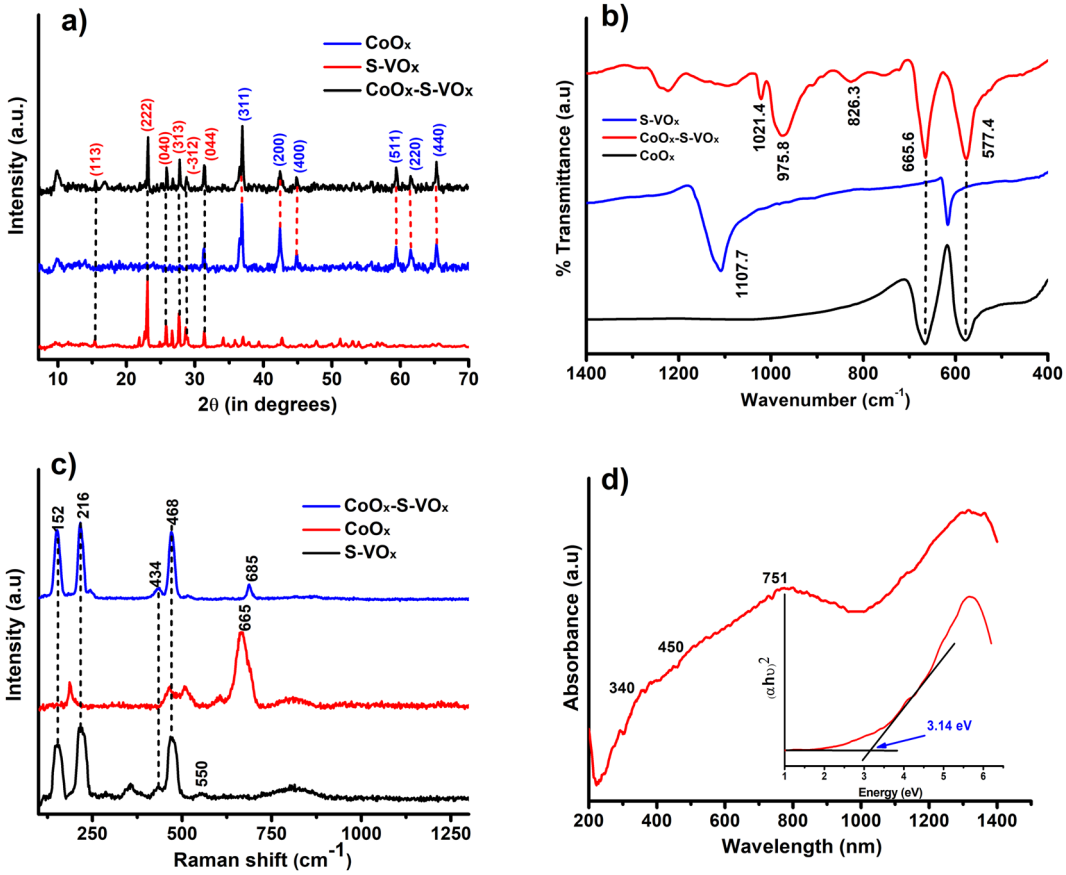

Fig. 1 (a) XRD pattern of CoO_x (blue), S–VO_x (red) and CoO_x–S–VO_x(black). (b) FTIR spectra of CoO_x (black), S–VO_x (blue) and CoO_x–S–VO_x (red). (c) Raman spectra of CoO_x (red), S–VO_x (black) and CoO_x–S–VO_x (blue) and (d) DRS spectra of CoO_x–S–VO_x, with the inset showing Tauc plot.

cobalt. The diffused reflectance spectrum (DRS) of CoO_x–S–VO_x as depicted in Fig. 1d showed three broad signals at 340 nm (a charge transfer band of ligand-metal cation V^{+5}), 450 nm (due to $O^{2-} \rightarrow Co^{2+}$ charge transfer transition) and 751 nm (due to $O^{2-} \rightarrow Co^{3+}$ charge transfer transition).[59,60]The material's band gap was determined using Tauc plot and was found to be ~3.14 eV as shown in Fig. 1d. The occurrence of a band gap smaller than 4 eV signified that our synthesized material could absorb the UV light of the solar spectrum. The DRS plot (Fig. S1a and b, ESI†) and band gap (Tauc plot) (Fig. S1c and d, ESI†) of the other two materials CoO_x and S–VO_x, respectively, are depicted in Fig. S1 of the ESI.†

The X-ray photoelectron spectroscopy (XPS) study was performed for CoO_x–S–VO_x and the respective spectra are shown in Fig. 2a–d. The XPS spectrum of V (2p) depicted in Fig. 2a exhibited the V (2p) signals for V ($2p_{1/2}$) and V ($2p_{3/2}$) with binding energy (B.E) values of 522.6 eV and 515.4 eV, respectively, characteristic of vanadium(IV) species. Two peaks at 528.3 eV and 529.3eV originated from the O (1s) peak of vanadium oxide species.[61] The B.E. values of Co ($2p_{3/2}$) and Co ($2p_{1/2}$) obtained at 780.3 eV and 796 eV, respectively, were assigned to Co^{+2} species while those at 778.5 eV and 793.5 eV were for Co^{+3} species. Along with these, the two satellite peaks at 786.2 eV and 802.5 eV resembled the spinel Co_3O_4 (Fig. 2b).[46,62] In the S(2p) spectrum as shown in Fig. 2c, a doublet was obtained at 161.8 eV and 163.1 eV that indicated the formation of S(0) species and another doublet at 165.6 eV and 166.7 eV corresponded to the oxidize form of sulfur.[63] The O (1s) binding energies were observed at 528.2 eV and 529.2 eV, signifying the formation of metal oxides (Fig. 2d). The XPS peaks were fitted with respect to C (1s) binding energy values as provided in Fig. S2 of the ESI.†[64]

The formation of vanadium(IV) species was again confirmed by the electron paramagnetic resonance (EPR) study. The presence of a hyperfine structure for vanadium ($I = 7/2$) clearly indicated the occurrence of vanadium(IV) oxide with the CoO_x matrix (Fig. S3a, ESI†).[65] The thermal stability of the synthesized materials was determined using thermo gravimetric analysis (TGA). The TGA of the synthesized CoO_x–S–VO_x (red) and S–VO_x (black) is shown in Fig. S3b (ESI†). The weight loss of 17.45% and 95.1% was observed from 150 °C to 250 °C in CoO_x–S–VO_x (red) and S–VO_x, respectively. This weight loss was attributed to the sublimation of inorganic sulfur, leading to the formation of residual metal oxides.[66] Also from the analysis, it was found that the thermal stability of S–VO_x was enhanced on mixing CoO_x.

From the scanning electron microscopy (SEM) analysis, we could see the formation of zeolitic-like crystals of the CoO_x–S–VO_x material (Fig. 3a–c). This was expected as we followed a zeolitic-imidazolate framework (ZIF) template approach during

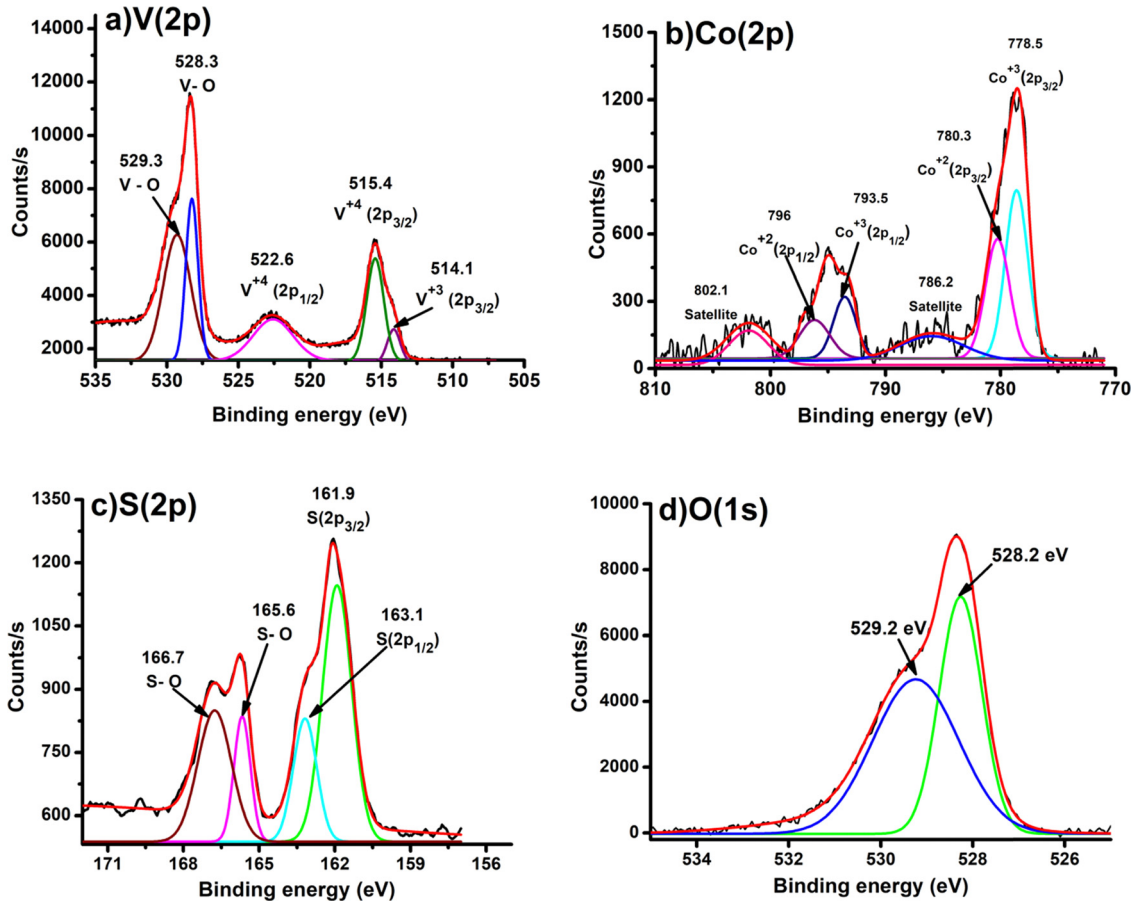

Fig. 2 XPS spectra of (a) V(2p), (b) Co(2p), (c) S(2p), and (d) O(1s) present in CoO_x–S–VO_x.

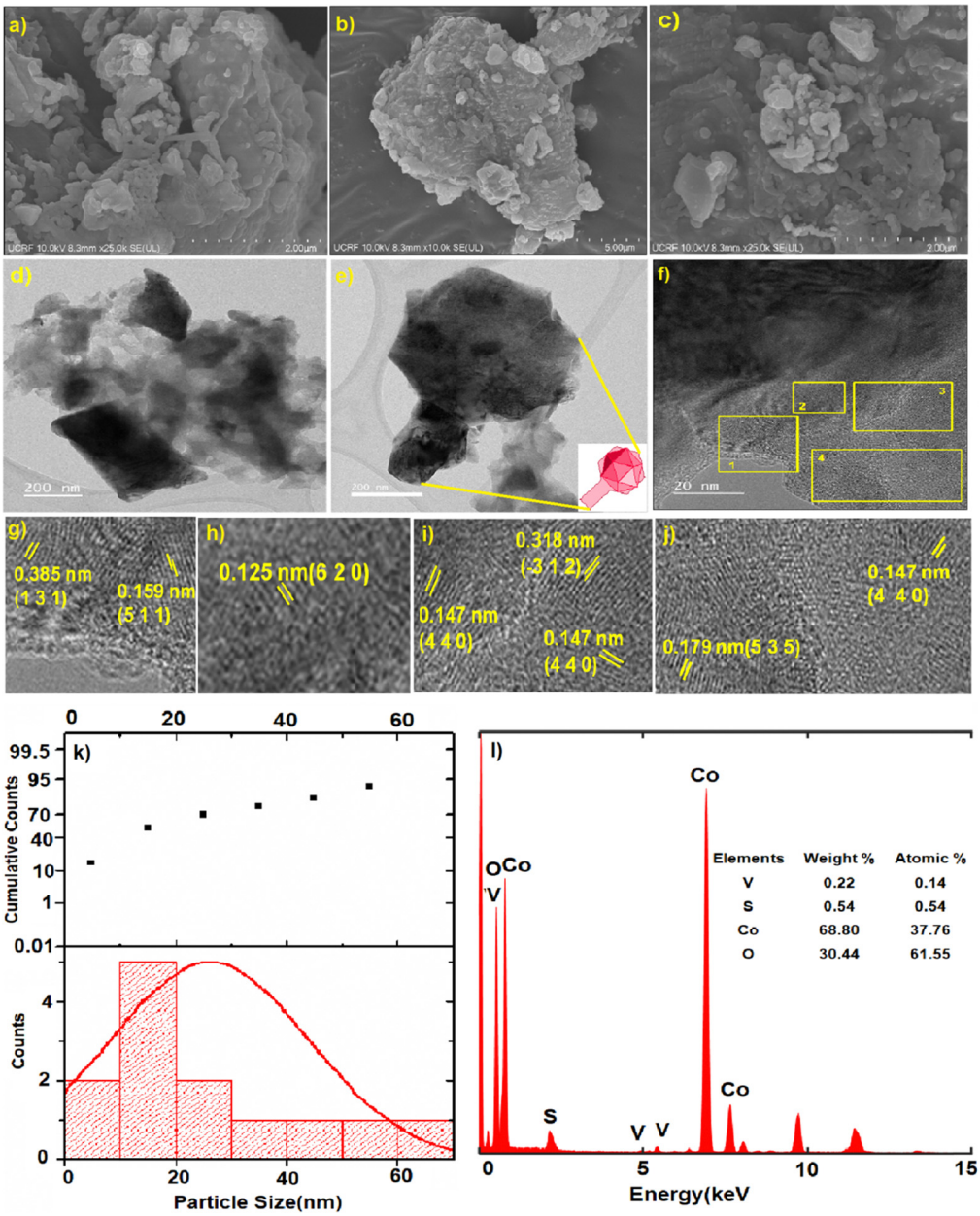

Fig. 3 (a)–(c) SEM images of the CoO_x–S–VO_x material, (d)–(f) TEM images, (g)–(j) are enlarged images marked as 1–4 in f, (k) particle size distribution curve, (l) the EDX spectra showing the elemental distribution in the catalyst.

our synthesis.[57,67] The ZIF-like structure was also seen from transmission electron microscopy (TEM) images (Fig. 3d and e). The SEM image (Fig. 3b) and the TEM image (Fig. 3e) represented an icosahedral-like morphology of the material.[68] The *d*-spacing values were calculated for the regions marked as 1–4 in Fig. 3f. The enlarged version of these regions is shown individually in Fig. 3g–j. The *d*-spacing values of 0.385 nm and 0.159 nm correspond to the (131) and (511) plane of sulfur (S_8) and Co_3O_4, respectively (Fig. 3g). The *d*-spacing values of 0.125 nm and 0.147 nm were assigned to the (620) and (440) planes of Co_3O_4 (Fig. 3h–j). The same with a *d*-spacing value of 0.318 nm was for the (−312) plane of V_3O_7 (Fig. 3i) and that with a d-value of 0.179 nm was for the (535) plane of S_8 (Fig. 3j). The planes were assigned with reference to the JCPDS card numbers used in the XRD analysis. From the particle size distribution (PSD) analysis (Fig. 3k), the size of the nanoparticle was found to be 20–35 nm. From the EDX analysis, the average weight percentage of the constituent atoms was found to be 27.43% (Co), 12.54% (V), 46.10% (S), and 13.91% (O), as shown in Fig. 3l. The atomic percentage ratio of Co and V was found to be 1.8 : 1. The scanning transmission electron microscopy high-angle annular dark-field (STEM-HAADF) images clearly indicated that the icosahedral was mostly comprised of cobalt oxide with vanadium and sulfur (Fig. 4a–f). The elemental analysis and EDX mapping were also performed in different regions of the nanocrystal and are provided in the ESI† (Fig. S4).

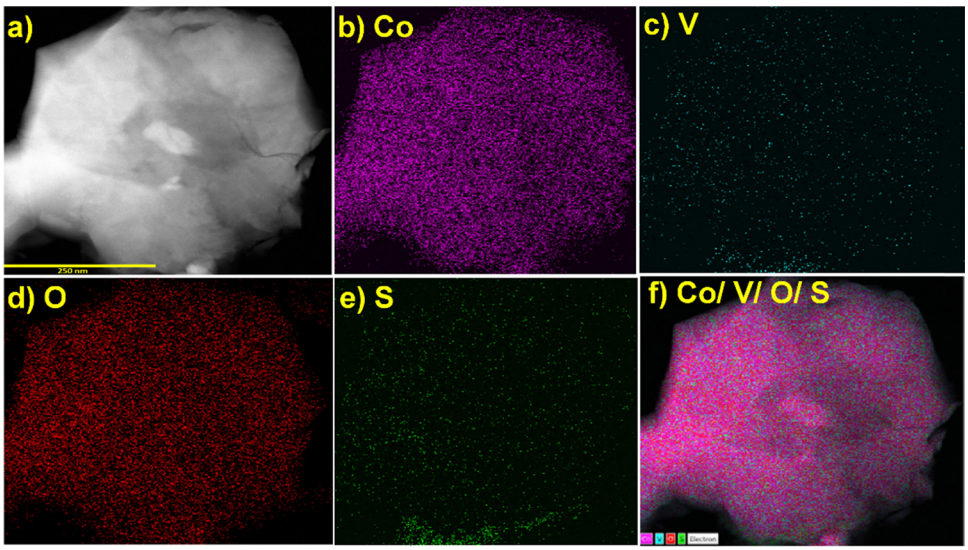

Fig. 4 (a) Region selected for STEM-HAADF-EDX mapping of the CoO_x–S–VO_xmaterial showing the presence of all the elements, (b) Co, (c) V, (d) O, (e) S, (f) mixing of all elements.

4. Reduction of Cr(VI)

The synthesized catalysts (CoO_x–S–VO_x, S–VO_x and CoO_x) were employed for the elimination of Cr(VI) ions from water. For this, a potassium dichromate ($K_2Cr_2O_7$) solution with a concentration of 50 ppm was prepared. The initial assessment of the three catalysts for Cr(VI) removal without the external reducing agent was found to be negative. Our previous studies and various other literature reports predicted that $NaBH_4$ served as a suitable reducing agent with an active catalyst for Cr(VI) reduction.[18,19,27] Therefore, considering 0.1 mmol of $NaBH_4$, 10 mL of Cr(VI) solution and 2 mg of CoO_x–S–VO_x catalyst, essential reaction parameters (time, $NaBH_4$ amount, and catalyst amount) were optimized for Cr(VI) reduction. From the graph shown in Fig. 5a, three minutes (3 min) of reaction time was found to be optimum and from the graphical representation shown in Fig. 5b, maximum of 49.14% of Cr(VI) got reduced. The percentage of Cr(VI) reduction was calculated by using eqn (1). As the Cr(VI) reduction percentage was comparatively lower than most of the reported ones, the same experiment was again analyzed by varying the concentration of $NaBH_4$. From the graphs (Fig. 5c and d), it was ascertained that 2 mg of the catalyst and 3 min of reaction time and 1 mmol of $NaBH_4$ were required to improve the Cr(VI) reduction percentage from 49.14 to 60.34%. Further enhancement of $NaBH_4$ concentration up to 2 mmol did not influence the Cr(VI) reduction process.

After getting the optimum time period and $NaBH_4$ concentration, the amount of catalyst was varied as it played a crucial role in the Cr(VI) reduction process as the Cr(VI) reduction process was negative only with $NaBH_4$. The catalyst amount was varied from 2 to 14 mg and the results are shown in Fig. 5e and f. It was observed that 10 mg of the catalyst resulted in 99.77% conversion of Cr(VI) to Cr (III). As a result of the aforementioned optimization, it was found that almost 100% of the Cr(VI) solution got reduced to Cr(III) within 3 min using 10 mg of the catalyst and 1 mmol $NaBH_4$. The reduction of Cr(VI) was mostly confirmed with the consecutive diminishing and disappearance of UV peaks at 271 nm and 372 nm. This was further validated by the colour change of the Cr(VI) solution from light yellowish to colourless. In order to study the reaction kinetics of Cr(VI) reduction, UV spectra were recorded every 30 sec. The rate constant determined using the first order rate-law was k (rate constant) = 0.0334 min^{-1} (Fig. S5a and b, ESI†).[69]

Under the optimized conditions, the catalyst was further tested by varying the Cr(VI) concentration. The study predicted that the catalyst was capable of reducing Cr(VI) with same competency up to 50 ppm. However, on further increasing the strength of Cr(VI) to 250 ppm, its efficiency decreased to 56.28% (Fig. S6a and b, ESI†). As suggested by the environmental protection agency's (EPA) study, the toxicity limit of Cr(VI) is 0.1 ppm, so it can be said that our synthesized catalyst CoO_x–S–VO_x can serve as a suitable material for Cr(VI) reduction up to a very high concentration of 50 ppm with almost 100% efficiency and within a very short period of time (3 min). It was interesting to observe that CoO_x–S–VO_x was only able to reduce Cr(VI); however the other catalysts, CoO_x, S–VO_x and Co_3O_4–V_2O_5 were found to be ineffective under the optimized condition (Fig. S7a and b, ESI†). It was attributed to the fact that the single metal catalysts S–VO_x and CoO_x as well Co_3O_4–V_2O_5 could not provide the sufficient number of electrons, which was required for the reduction of Cr(VI) to Cr(III).

5. Mechanism of Cr(VI) reduction

When potassium dichromate ($K_2Cr_2O_7$) is dissolved in water, an equilibrium is created between the dichromate ($Cr_2O_7^{2-}$) and chromate (CrO_4^{2-}) ions as follows.[70]

$$Cr_2O_7^{2-} + H_2O \rightleftarrows 2CrO_4^{2-} + 2H^+ \quad (2)$$

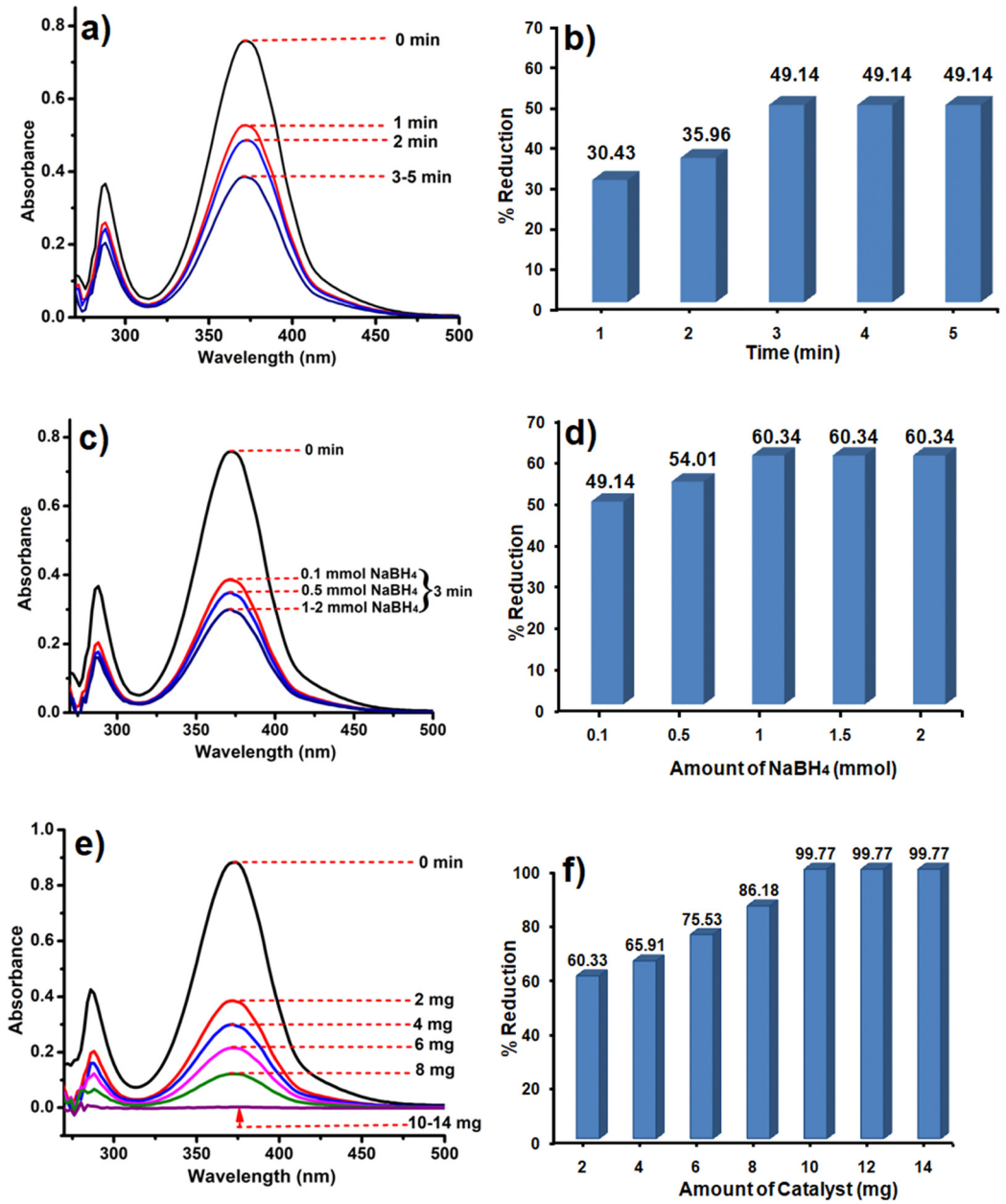

Fig. 5 UV spectra and bar diagram showing the dependency of Cr(VI) reduction on time (a) and (b), $NaBH_4$concentration (c) and (d) and catalyst amount (e) and (f).

Such types of equilibrium were found to be dependent on pH of the solution.[71] In the presence of our catalyst, the pH of the solution was 7.05, while it was 6.17 for aqueous $K_2Cr_2O_7$ solution. At this pH, the equilibrium equation becomes,

$$CrO_4^{2-} + 2H^+ \rightleftarrows HCrO_4^- \quad (3)$$

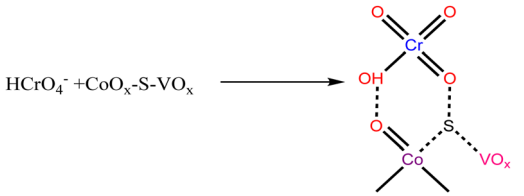

(4)

The $HCrO_4^-$ species was expected to interact with the catalyst as shown in eqn (4). This $HCrO_4^-$ species is reported to have a redox potential of +1.35 V.[72] Therefore, it is considered to be highly reducible in the presence of the species that can behave as a Lewis base or an electron donor. In this case, the low valent V^{+4}, Co^{+2} and S atoms can serve as an electron donor center and the required H^+ ions will be provided by $NaBH_4$. So, the reduction of Cr(VI) can be expressed by the following reactions.[73]

Hydrolysis of $NaBH_4$:

$$NaBH_4 + 2H_2O \rightarrow NaBO_2 + 4H_2 \quad (5)$$

$$BO_2^- + 2H_2O \rightarrow H_3BO_3 + OH^- \quad (6)$$

$$H_3BO_3 + H_2O \rightarrow B(OH)_4^- + H^+ \quad (7)$$

Reduction of Cr(VI):

$$HCrO_4^- + 7H^+ + 3e^- \rightarrow Cr^{+3} + 4H_2O \quad (8)$$

The reduction process was evaluated through the cyclic voltametric study (Fig. S8, ESI†). The cyclic voltamogram (CV) of the $K_2Cr_2O_7$ solution represented a sharp cathodic peak at −0.24 V, and the potential value matches the reported one for CrO_4^{2-}.[74] This indicated that in an aqueous medium, $Cr_2O_7^{2-}$ ionizes to CrO_4^{2-}. On addition of the catalyst, almost a reversible couple with a sharp anodic peak at +0.83 V *vs.* Ag/AgCl (+1.03 V *vs.* NHE) was observed. This anodic peak matched the reported redox potential value for $HCrO_4^-$ species.[75] After addition of $NaBH_4$, the anodic peak for $HCrO_4^-$ got diminished and the voltamogram represented the hydrogen evolution reaction due to the reduction of H^+ ions. The CV analysis was in accordance with our proposed mechanism, thereby proving the efficacy of our catalyst for Cr(VI) reduction.

6. Degradation of methyl orange (MO)

Like Cr(VI), there are many other organic dye components which are released from textile industries to nearby water bodies.[76] One of such examples is the contamination of Yamuna river located in New Delhi, India.[77] Therefore, the removal of dye contaminants for waste water treatment especially in the industrial urban areas is the need of the present environmental situation. After going through the literature, it is realized that the different catalysts or photocatalysts are designed, which are either effective for Cr(VI) reduction or for different dye degradation processes. But reports on single catalysts that have the potential to reduce Cr(VI) to Cr(III) as well as degrade dyes like MO are very less. MO is an anionic dye which is more frequently used in textile industries. They are toxic in nature if present in high concentration, so they need to be decomposed to CO_2 and H_2O.

Initially, the reaction was studied using 5 mg of the CoO_x–S–VO_x catalyst and the dye degradation process was monitored through UV-visible spectroscopy. It was found that with 5 mg of the catalyst, only 42.83% of the dye got degraded in 15 min (Fig. 6a and b). Increasing the light irradiation time did not improve the percentage of degradation. Therefore, considering 15 min to be optimized light irradiation time, the catalyst amount was changed from 5 to 15 mg and found that the degradation process completed with 99.40% (Fig. 6c and d). Furthermore, increase in the catalyst amount did not improve the percentage of degradation. So, 15 mg of the catalyst and 15 min of light irradiation time were considered optimum reaction parameters. To fix the degradation kinetics, UV spectra were recorded after an interval of 3 min (Fig. 7a). The plot of $\ln(C_o/C_t)$ *vs.* time generated a linear line plot, suggesting a 1st order kinetics with the rate constant (k) of 0.46238 min^{-1} for the MO dye degradation process (Fig. 7b).[78]

In the usual process, the decolourization of the dye and change in the absorbance value in the UV-visible spectrum do not signify the decomposition of dye into H_2O and CO_2. This is one of the challenging issues in the dye degradation process. Therefore, to validate that the synthesized catalyst decomposes the dye, the total organic content (TOC) over different time intervals under optimized conditions (15 mg of the catalyst CoO_x–S–VO_x) was calculated. The TOC was determined using

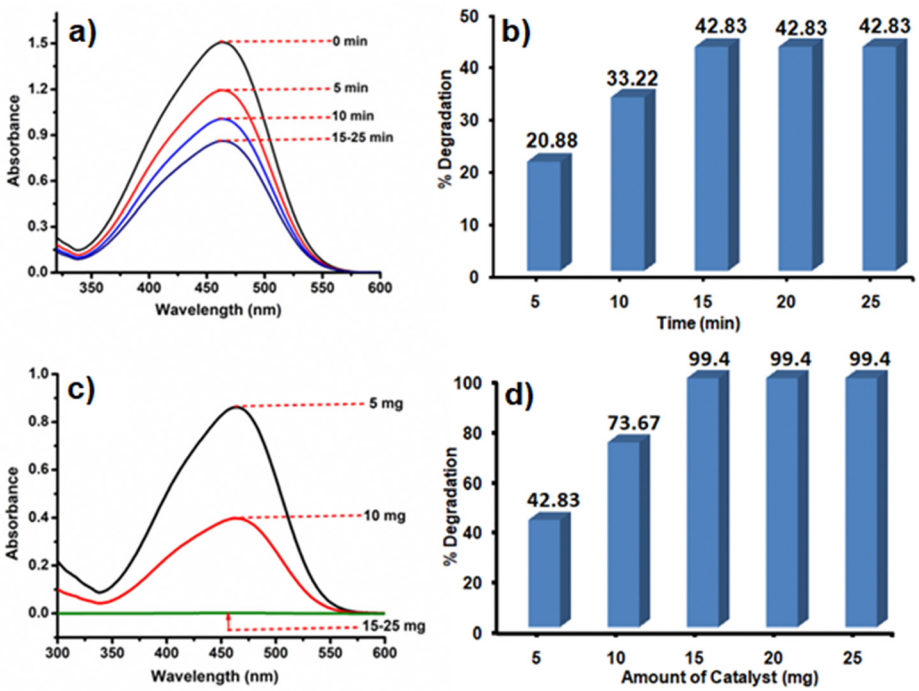

Fig. 6 UV spectra and bar diagram showing the dependence of MO degradation on time (a) and (b), and catalyst amount (c) and (d).

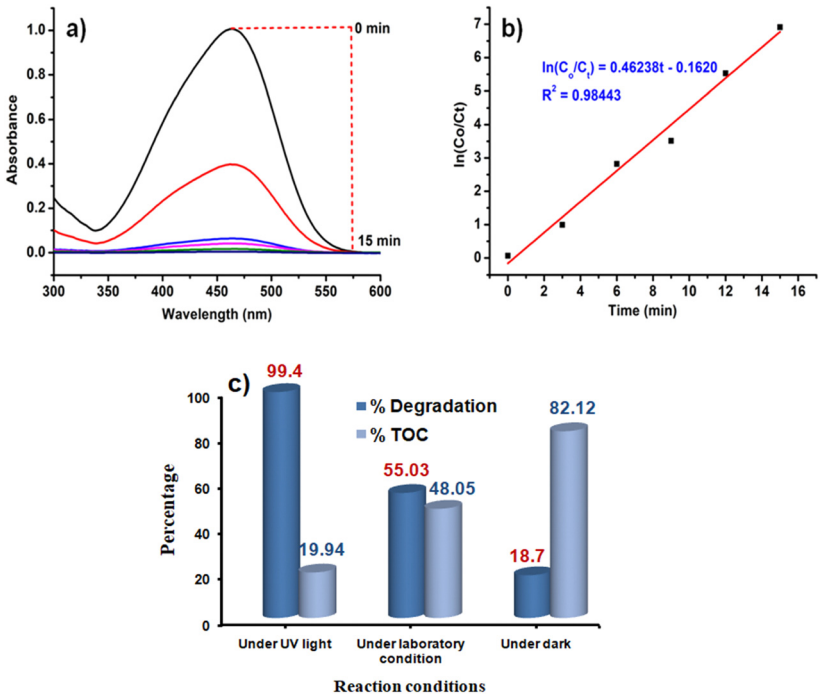

Fig. 7 (a) UV spectra recorded over a 5 min time interval under optimized reaction conditions, (b) $\ln(C_o/C_t)$ *vs.* time graph depicting a kinetic mechanism for MO degradation, and (c) comparative bar diagram of TOC and percentage degradation under various conditions.

the Walkley and Black method as previously stated by our group.[79] The TOC was found to be 19.94% after the completion of the reaction under UV-light irradiation and suggested that percentage of degradation and decomposition was not the same (Fig. 7c). This reveals the fact that the catalyst was able to mineralize 80.06% of the total dye content to CO_2 and H_2O under the photocatalytic condition.

In order to confirm that dye degradation was occurring in the presence of light, the same reaction was performed under the optimized condition without UV-light irradiation. For this, the reaction mixture was stirred for 15 min under normal laboratory surrounding and dark conditions (Fig. S9a and b, ESI†). It was found that under this condition, the percentage degradation and TOC, respectively, were found to be 55.03% and 48.05% under normal laboratory conditions and 18.7% and 82.12% under dark conditions (Fig. 7c). It is pertinent to mention that when the reaction was carried out under normal conditions under stirring for 40 min, degradation was improved to 72.27%. Similarly, under dark conditions, degradation was found to be 33.92% after 40 min (Fig. S9c, ESI†). However, no further improvement was observed on performing the reaction for longer period. This implied that UV-light irradiation significantly facilitated the degradation of dye and its decomposition.

After finding the CoO_x–S–VO_x catalyst to be an effective catalyst for MO degradation, the other catalysts named Co_3O_4–V_2O_5, S–VO_x and CoO_x were also tested for MO degradation with 15 mg of the catalyst (Fig. S10a and b, ESI†). Co_3O_4–V_2O_5, S–VO_x and CoO_x could degrade only 22.72%, 39.39% and 51.55% MO dye, respectively, upon irradiation for 40 min. There may be two reasons for such ineffectiveness, one Co_3O_4–V_2O_5 and S–VO_x exhibited a high band gap of 3.38 eV and 4.8 eV, respectively, while CoO_x had a band gap of 3.32 eV but probably could not separate the electron–hole (e^-–h^+) pair effectively, leading to its low activity.[49] Since a greater amount of MO is released into the water system, a study was performed to determine the effectiveness of our catalyst at higher molar concentrations of MO. Under the optimized condition, on increasing the dye concentration from 10^{-6} to 10^{-3} M, the degradation percentage got lowered to 33.22% (Fig. S11a and b, ESI†).

7. Point of zero charge (PZC) and Effect of pH on the degradation of MO

7.1. Determination of PZC of CoO_x–S–VO_x

Point of zero charge (PZC) of our synthesized catalyst was evaluated using the reported batch equilibrium method.[80] For this, a solution of sodium chloride (0.1 M) was prepared and 20 mL of NaCl solution was taken in each of six beakers. Using 0.1 M H_2SO_4 or 0.1 M KOH, the pH of the solutions was changed to different pH values. 5 mg of the CoO_x–S–VO_x catalyst was added to each beaker, which was then stirred for 24 h, and then filtered and final pH values of all solutions were recorded after 24 h. By plotting the difference in the pH value against the initial pH value, the PZC of the catalyst was found to be 4 (Fig. S12a, ESI†).

7.2. Effect of pH on the degradation of MO

To evaluate the effect of pH, six different solutions of 10^{-6} M MO were taken, and pH of each solution was calibrated to 2, 4,

6, 8, 10 and 12 using 0.1 M KOH and 0.1 M H_2SO_4. Under the different pH conditions, photocatalytic degradation was carried out with the optimized reaction parameters and the recorded results are given in Fig. S12b (ESI†). Degradation efficiency was found to decrease from 99.77% to 65% with an increase in pH from 2 to 12. This can be explained from the PZC value of the synthesized catalyst. When pH < PZC, the material acquired a net positive charge on its surface. As a result, the negatively charged MO dye molecules were more attracted to the positively charged catalyst surface, thereby enhancing the rate of degradation. Because of this reason, when pH > PZC, the rate of MO dye degradation got retarded at higher pH.[80]

8. Mechanistic study of dye degradation

The mechanism of dye degradation was believed to proceed *via* the excitation of electrons from the conduction band (CB) to the valence band (VB) of CoO_x–S–VO_x as shown in Fig. 8a. As the catalyst possessed an appropriate band gap of 3.14 eV, this electron transfer process creating the positive holes at the CB was expected to occur prominently. In general, in spite of having a suitable band gap, a catalyst may not perform well during photocatalytic dye degradation if the rate of electron and hole recombination was very fast and this can be a probable reason for the observed behavior of our synthesized material CoO_x. Devi *et al.* have reported that the presence of a sulfur atom can help in separating the electrons and holes by oxidizing itself to SO_4^{2-} ions and serving as an electron trapping agent, as shown in Fig. 8a.[81] As the present S–VO_x catalyst possessed an inorganic sulfur atom, from the XPS analysis, it was observed that under an oxidizing environment, it can oxidize to SO_4^{2-}. Therefore, it was believed that in the present case, the sulfur atom oxidizes to SO_4^{2-} ions and trapped the electron in the CB and thereby favored the photodegradation process keeping the holes (h^+) free from negatively charged electrons. It was also reported that the SO_4^{2-} ion can draw electrons from Lewis acidic sites through the inductive effect of S = O.[81] As a result, Lewis acidic sites are transformed to Brønsted acidic sites (BAS). The BAS then abstracted a proton from the water and created more hydroxyl (OH^-) ions which then combined with the holes to produce more hydroxyl radicals ($OH^•$). So probably in our catalyst having the V^{+4} and Co^{+3} sites may transform to BAS through the inductive effect of *in situ*-created SO_4^{2-} ions and increased the generation of $OH^•$. The high valent Lewis acidic sites on the catalyst surface may also help in electron trapping as the Co^{+3} ion can fluctuate in

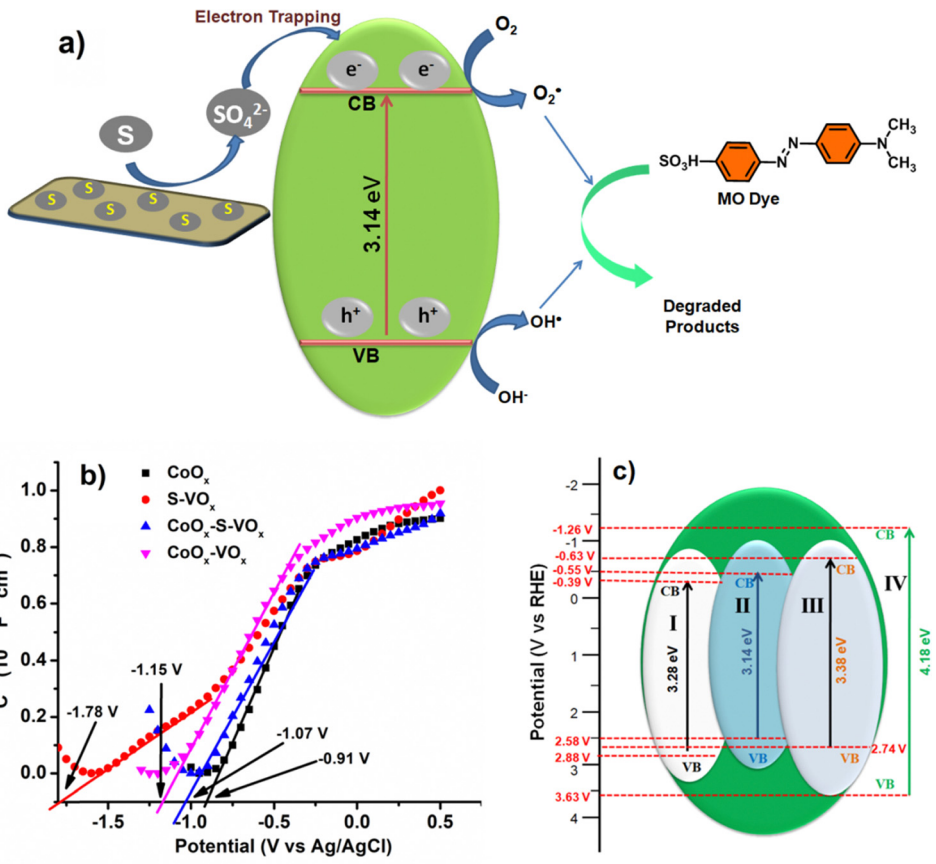

Fig. 8 (a) Plausible charge transfer routes for the CoO_x–S–VO_x material, (b) Mott–Schottky (flat band potential) and (c) band edge structure plot of all the catalysts, (I) CoO_x (II) CoO_x–S–VO_x, (III) Co_3O_4–V_2O_5, (IV) S–VO_x. [Flat band potential (E_{FB}) = Conduction band potential (E_{CB}) + 0.1 V, Valance band potential (E_{VB}) = Band gap + E_{CB}].[83]

between Co^{+2} and Co^{+3}. Therefore, it can be said that the presence of a S atom with the conjugate metal oxide (VO_x–CoO_x) not only manifested a suitable band gap in the photocatalyst but also helped in electron–hole separation by converting itself to an electron scavenging agent.

The photoluminescence (PL) spectroscopy analysis was performed with an excitation radiation of 450 nm and 740 nm (Fig. S13a and b, ESI†). When excited at 450 nm, CoO_x–S–VO_x showed emission bands at 687 nm and 1030 nm and S–VO_x showed emission bands at 700 nm and 1057 nm, and CoO_x did not show any emission band at this excitation wavelength. Similarly, when excited at 740 nm, both CoO_x–S–VO_x and CoO_x showed emission signals at 905 nm, and S–VO_x did not show any emission band upon excitation at 740 nm. The difference in the photoluminescence behavior was attributed to the difference in the absorption band as obtained from DRS analysis (Fig. 1d and Fig. S1a, b, ESI†). The appearance of the near infrared (NIR) emission band was attributed to the presence of electronic transitions at higher wavelength as observed from the DRS spectra (Fig. S1a and b, ESI†). It was observed from the PL spectra analysis that the intensity of the emission signal for CoO_x–S–VO_x appearing at 905 nm had low intensity compared to CoO_x. Similarly, the emission band above 1000 nm also showed lowering of intensity in comparison with S–VO_x. This indicated that the electron–hole recombination rate was suppressed in the case of CoO_x–S–VO_x in comparison with CoO_x and S–VO_x. This implied that CoO_x–S–VO_x can serve as a better photocatalyst in MO dye degradation by relaxing the electron–hole recombination rate.[82]

To further have a proper understanding of the mechanism, we also calculated the valence band position and conduction band position using the Mott–Schottky (MS) plot (Fig. 8b). MS plots were obtained by performing electrochemical impedance spectroscopy (EIS) over a range of applied potential values. The flat band potential (V_{fb}) values of the materials CoO_x, S–VO_x, Co_3O_4–V_2O_5 and CoO_x–S–VO_x were estimated by extrapolating the linear region of the MS plot. The obtained V_{fb} values of CoO_x, S–VO_x, Co_3O_4–V_2O_5 and CoO_x–S–VO_x were −0.91 V, −1.78 V, −1.15 V and −1.07 V, respectively *vs.* Ag/AgCl electrode. The $1/C^2$ *vs.* V plots for all the materials exhibited positive slopes, indicating n-type semiconductor properties of the materials. Therefore, CB band position and VB position of the materials were calculated by combining the band gap (E_g) values obtained from DRS analysis and V_{fb} values obtained from MS plots, as shown in Fig. 8c. The CB position along with the VB position for all the synthesized catalysts are shown in Fig. 8c.[83,84] From the diagram, it was observed that the CoO_x–S–VO_x catalyst had a CB potential that was slightly more negative than the $O_2/O_2^{-\bullet}$ potential *vs.* NHE (−0.46 V). Similarly, the VB was approximately in the range of oxidation potential of $H_2O/OH^\bullet$. This further implied that our synthesized catalyst can effectively produce hydroxyl radicals ($OH^\bullet$) or $O_2^{-\bullet}$ and can degrade the dye effectively. In contrast, the band edge potential for the other two catalysts differs significantly, especially in the case of S–VO_x making it unsuitable for the photodegradation process. The same applies to Co_3O_4–V_2O_5 indicating the role of sulfur in modulating the band gap potential and thereby making the CoO_x–S–VO_x catalyst most suitable for the photodecomposition of MO. Although CoO_x possessed CB position within the limit of water splitting reaction, probably as mentioned earlier due to non-availability of any electron scavenging agent, it did not participate well in the photooxidation process. The VB of the most effective catalyst (CoO_x–S–VO_x) was also calculated using UPS analysis shown in Fig. S14a and b (ESI†). It was found to be 2.8 eV approximately equivalent to that calculated from the MS plot. The work function was found to be 5.5 eV and was in the range of work function for cobalt oxide and vanadium oxide.[85]

Based on the proposed mechanism, it was understood that the photodegradation process probably proceeded either through the creation of hydroxyl radicals ($OH^\bullet$) or superoxide radicals ($O_2^{-\bullet}$). So, in order to verify the involvement of such radical species, the photodegradation process was again studied by using some scavenging agents. Potassium iodide (KI) was used as a hole scavenging agent, silver nitrate ($AgNO_3$) as an electron scavenging agent, isopropanol and ascorbic acid were used as $OH^\bullet$ and $O_2^{-\bullet}$ radical scavenging agents, respectively.[82] From the graph shown in Fig. S15 (ESI†), it was found that the efficacy in the presence of holes and electron scavengers remained almost the same, while it got retarded in the presence of radical scavengers. This implied that the radicals either $O_2^{-\bullet}$ or $OH^\bullet$ were the active species for the decomposition of anionic MO dye.

9. Recyclability test

In order to check recyclability, the CoO_x–S–VO_x material was considered as the test catalyst and performed both Cr(VI) reduction and MO dye degradation reaction. Both the reactions were carried out up to 10th cycle. After 2nd cycle, 95% and 93% efficiency was observed in the case of Cr(VI) reduction and MO degradation reaction, respectively. Further decrease in efficiency was observed in the consecutive cycles as shown in Fig. S16 (ESI†). However, the decreasing rate was not significantly higher and ranged from 90 to 75% until the 10th cycle. These investigations revealed that the synthesized CoO_x–S–VO_x material was stable and could be recycled ten times without causing any substantial loss in efficiency. After 10th cycle, the remaining material was collected and then PXRD analysis (Fig. S17, ESI†), SEM and TEM analysis (Fig. S18, ESI†) were performed. The PXRD analysis of the recycled catalyst indicated the loss in the crystallinity of the original catalyst and probably influenced the catalytic activity. Similarly, from the SEM and TEM analysis, a change in the morphology of CoO_x–S–VO_x and a decrease in the presence of fine nanoparticles were observed leading to loss of activity. Thus, it can be said that the change in the catalyst structure and morphology resulted in the decrease of degradation activity for Cr(VI) reduction and MO dye degradation reaction.

10. Conclusion

In summary, it can be said that the synthesized mixed metal oxide catalyst of cobalt and vanadium doped with inorganic

sulfur served as a catalyst for Cr(VI) reduction as well as for MO dye degradation. The reduction of Cr(VI) to Cr(III) was found to be very fast in comparison to many other literature reports. The synthesized catalyst also appeared as a photocatalyst for the decomposition of MO dye harvesting the UV-light. The study predicted that the photocatalytic dye decomposition process was dependent on various parameters like time, catalyst amount, pH, and reaction environment. The dye degradation process was found to be more effective at low pH. The comparison of the activity of the bimetallic CoO_x–S–VO_x catalyst with its monometallic counterpart *viz* CoO_x and S–VO_x indicated that the mixed metal oxide was highly effective in comparison to the single metal oxides. The band structure of the catalysts was correlated with the mechanism of the photocatalytic process through various analyses. The mechanistic understanding revealed the dominant role of radicals in the photocatalytic process. The catalyst reduced Cr(VI) to Cr(III) even at a higher concentration level in very less time (3 min) and very effectively decomposed the toxic industrial waste dye with high mineralization percentage. Therefore, the present study can offer a new direction and perspective for sustainable development and the elimination of environmental pollutants, including toxic metals like hexavalent chromium.

Author contributions

Sayanika Saikia: methodology, validation, formal analysis, investigation, writing – review & editing; Manoshi Saikia: formal analysis, writing – review & editing; Salma A. Khanam: formal analysis, investigation; Seonghwan Lee: resources, formal analysis; Young-Bin Park: resources, formal analysis; Lakshi Saikia: resources, formal analysis; Gautam Gogoi: validation, formal analysis; Kusum K. Bania: conceptualization, writing – original draft, writing – review & editing visualization, supervision, project administration, funding acquisition.

Conflicts of interest

There are no conflicts to declare.

Acknowledgements

KKB acknowledges SERB for the research grant (CRG/2019/000962) and CSIR (NO. 80(0094)/20/EMR-II). S. Saikia acknowledges University Grants Commission (UGC) for the Junior Research Fellowship. The authors also acknowledge Tezpur University for offering the analytical and infrastructural facilities required for this research work.

References

1 S. Rojas and P. Horcajada, *Chem. Rev.*, 2020, **120**, 8378–8415.
2 C. O. Okoye, C. I. Addey, O. Oderinde, J. O. Okoro, J. Y. Uwamungu, C. K. Ikechukwu, E. S. Okeke, O. Ejeromedoghene and E. C. Odii, *Chem. Eng. J. Adv.*, 2022, **11**, 100310.
3 M. Sajid, M. K. Nazal, N. Baig and A. M. Osman, *Sep. Purif. Technol.*, 2018, **191**, 400–423.
4 A. D. Bokare and W. Choi, *Environ. Sci. Technol.*, 2010, **44**, 7232–7237.
5 J. A. Jacobs and S. M. Testa, *Overview of chromium(VI) in the environment: background and history*, CRC Press, 2005, pp. 1–21.
6 M. Owlad, M. K. Aroua, W. A. W. Daud and S. Baroutian, *Water, Air, Soil Pollut.*, 2009, **200**, 59–77.
7 L. S. McNeill, J. E. McLean, J. L. Parks and M. A. Edwards, *J. Am. Water Works Assoc.*, 2012, **104**, E395–E405.
8 P. Veerakumar, P. Thanasekaran, K. C. Lin and S. B. Liu, *ACS Sustainable Chem. Eng.*, 2017, **5**, 5302–5312.
9 R. M. Sedman, J. A. Y. Beaumont, T. A. McDonald, S. Reynolds, G. Krowech and R. Howd, *J. Environment. Sci. Health C*, 2006, **24**, 155–182.
10 S. W. Hu, L. W. Yang, Y. Tian, X. L. Wei, J. W. Ding, J. X. Zhong and P. K. Chu, *Appl. Catal. B: Environ.*, 2015, **163**, 611–622.
11 Y. Ying, Y. Liu, X. Wang, Y. Mao, W. Cao, P. Hu and X. Peng, *ACS Appl. Mater. Interfaces*, 2015, **7**, 1795–1803.
12 Y. Cheng, F. Yan, F. Huang, W. Chu, D. Pan, Z. Chen, J. Zheng, M. Yu, Z. Lin and Z. Wu, *Environ. Sci. Technol.*, 2010, **44**, 6357–6363.
13 H. L. Ma, Y. Zhang, Q. H. Hu, D. Yan, Z. Z. Yu and M. Zhai, *J. Mater. Chem.*, 2012, **22**, 5914–5916.
14 P. K. Boruah, P. Borthakur, G. Darabdhara, C. K. Kamaja, I. Karbhal, M. V. Shelke, P. Phukan, D. Saikia and M. R. Das, *RSC Adv*, 2016, **6**, 11049–11063.
15 B. Xie, C. Shan, Z. Xu, X. Li, X. Zhang, J. Chen and B. Pan, *Chem. Eng. J.*, 2017, **308**, 791–797.
16 J. Nan, S. Guo, D. Alhashmialameer, Q. He, Y. Meng, R. Ge, S. M. El-Bahy, N. Naik, V. Murugadoss, M. Huang and B. B. Xu, *ACS Appl. Nano Mater.*, 2022, **5**, 8755–8766.
17 B. Gopal and A. Gupta, *ACS Omega*, 2019, **4**, 20443–20449.
18 O. Njoya, S. Zhao, Y. Qu, J. Shen, B. Wang, H. Shi and Z. Chen, *J. Environ. Manage.*, 2020, **275**, 111165.
19 O. Njoya, S. Zhao, J. Shen, X. Kong, Y. Gong, B. Wang, J. Kang and Z. Chen, *Sep. Purif. Technol.*, 2022, **301**, 122051.
20 M. U. Rahman and S. A. Kazmi, *J. Chem. Soc. Pak*, 2011, **19**, 201.
21 X. R. Xu, H. B. Li, X. Y. Li and J. D. Gu, *Chemosphere*, 2004, **57**, 609–613.
22 Y. C. Zhang, J. Li, M. Zhang and D. D. Dionysiou, *Environ. Sci. Technol.*, 2011, **45**, 9324–9331.
23 W. Yang, L. Zhang, Y. Hu, Y. Zhong, H. B. Wu and X. W. Lou, *Angew. Chem.*, 2012, **124**, 11669–11672.
24 H. Abdullah and D. H. Kuo, *ACS Appl. Mater. Interfaces*, 2015, **7**, 26941–26951.
25 M. A. Pandit, D. S. H. Kumar, M. Ramadoss, Y. Chen and K. Muralidharan, *RSC Adv.*, 2022, **12**, 7762–7772.
26 M. Madkour, Y. Abdelmonem, U. Y. Qazi, R. Javaid and S. Vadivel, *RSC Adv.*, 2021, **11**, 29433–29440.
27 B. Das, M. Sharma, J. C. Sarmah and K. K. Bania, *J. Environ. Chem. Eng.*, 2017, **5**, 4212–4219.

28 R. Kamaraj and S. Vasudevan, *ChemistrySelect*, 2019, **4**, 2428–2435.
29 G. Liu, P. Niu, L. Yin and H. M. Cheng, *J. Am. Chem. Soc.*, 2012, **134**, 9070–9073.
30 J. Jiang, Z. Xiong, H. Wang, G. Liao, S. Bai, J. Zou, P. Wu, P. Zhangand and X. Li, *J. Mater. Sci. Technol.*, 2022, **118**, 15–24.
31 S. Lu, W. Liao, W. Chen, M. Q. Yang, S. Zhuand and S. Liang, *Appl. Surf. Sci.*, 2023, **614**, 156224.
32 T. Zhu, J. Pan, Z. An, R. Zhe, Q. Ou and H. E. Wang, *J. Mater. Chem. A*, 2022, **10**, 20375–20385.
33 S. Y. Xiao, Y. Liu, X. F. Wu, L. T. Gan, H. Y. Lin, L. R. Zheng, S. Dai, P. F. Liu and H. G. Yang, *J. Mater. Chem. A*, 2021, **9**, 14786–14792.
34 Y. F. Ren, Z. L. He, H. Z. Zhao and T. Zhu, *Rare Metals*, 2022, **41**, 830–835.
35 Y. Vasseghian, F. Almomani, M. Moradi and E. N. Dragoi, *J. Hazard. Mater.*, 2022, **423**, 127016.
36 Y. Vasseghian, E. N. Dragoi and F. Almomani, *Chemosphere*, 2022, **287**, 132387.
37 S. Moosavi, C. W. Lai, S. Gan, G. Zamiri, O. Akbarzadeh Pivehzhani and M. R. Johan, *ACS omega*, 2020, **5**, 20684–20697.
38 E. Routoula and S. V. Patwardhan, *Environ. Sci. Technol.*, 2020, **54**, 647–664.
39 R. Guo, T. Jiao, R. Li, Y. Chen, W. Guo, L. Zhang, J. Zhou, Q. Zhang and Q. Peng, *ACS Sustainable Chem. Eng.*, 2018, **6**, 1279–1288.
40 S. Rafaqat, N. Ali, C. Torres and B. Rittmann, *RSC Adv.*, 2022, **12**, 17104–17137.
41 A. Ajmal, I. Majeed, R. N. Malik, H. Idriss and M. A. Nadeem, *RSC Adv.*, 2014, **4**, 37003–37026.
42 Y. Wang, C. Liang, C. Fan, J. Chen, Z. Zhang and H. Liu, *Environ. Sci.: Nano*, 2023, **10**, 891–901.
43 C. Liu, X. Dong, Y. Hao, X. Wang, H. Ma and X. Zhang, *RSC Adv.*, 2017, **7**, 22415–22423.
44 A. Pirkarami and M. E. Olya, *J. Saudi Chem. Soc.*, 2017, **21**, S179–S186.
45 M. Nazim, J. H. Kim, H. Y. Lee and S. K. Cho, *Langmuir*, 2021, **37**, 12929–12939.
46 S. He, Y. Chen, X. Li, L. Zeng and M. Zhu, *ACS ES&T Eng*, 2022, **2**, 527–546.
47 J. Luo, S. Zhang, M. Sun, L. Yang, S. Luo and J. C. Crittenden, *ACS nano*, 2019, **13**, 9811–9840.
48 S. Gautam, H. Agrawal, M. Thakur, A. Akbari, H. Sharda, R. Kaur and M. Amini, *J. Environ. Chem. Eng.*, 2020, **8**, 103726.
49 M. J. Baruah, T. J. Bora, G. Gogoi, N. Hoque, N. K. Gour, S. K. Bhargava, A. K. Guha, J. K. Nath, B. Das and K. K. Bania, *J. Colloid Interface Sci.*, 2022, **608**, 1526–1542.
50 S. A. Khan, Z. Arshad, S. Shahid, I. Arshad, K. Rizwan, M. Sher and U. Fatima, *Compos. B: Eng.*, 2019, **175**, 107120.
51 M. A. Bhatti, A. A. Shah, K. F. Almani, A. Tahira, S. E. Chalangar, A. Dad Chandio, O. Nur, M. Willander and Z. H. Ibupoto, *Ceramics International*, 2019, **45**, 23289–23297.
52 D. Khalafallah, O. Y. Alothman, H. Fouad and K. A. Khalil, *Int. J. Hydrogen Energy*, 2018, **43**, 2742–2753.
53 M. M. Sajid, N. A. Shad, Y. Javed, S. B. Khan, Z. Zhang, N. Amin and H. Zhai, *Surf. Interfaces*, 2020, **19**, 100502.
54 R. Baddour-Hadjean, M. B. Smirnov, K. S. Smirnov, V. Y. Kazimirov, J. M. Gallardo-Amores, U. Amador, M. E. Arroyo-de Dompablo and J. P. Pereira-Ramos, *Inorg. Chem.*, 2012, **51**, 3194–3201.
55 Z. Wang, X. Li, W. Guo and Y. Fu, *Adv. Funct. Mater.*, 2021, **31**, 2009875.
56 M. S. Weimer, R. F. McCarthy, J. D. Emery, M. J. Bedzyk, F. G. Sen, A. Kinaci, M. K. Chan, A. S. Hock and A. B. Martinson, *Chem. Mater.*, 2017, **29**, 2864–2873.
57 X. Wu, J. Wang, S. Liu, X. Wu and S. Li, *Electrochim. Acta*, 2011, **56**, 10197–10203.
58 S. A. Khanam, N. Hoque, S. Lee, Y. B. Park, G. Gogoi and K. K. Bania, *ACS Appl. Energy Mater.*, 2022, **5**, 12651–12662.
59 T. V. Larina, S. V. Cherepanova, N. A. Rudina, B. A. Kolesov and A. N. Zagoruiko, *Catal. Sustainable Energy*, 2016, **2**, 87–95.
60 S. Ambika, S. Gopinath, K. Saravanan, K. Sivakumar, C. Ragupathi and T. A. Sukantha, *Energy Rep.*, 2019, **5**, 305–309.
61 T. Jenkins, J. A. Alarco, B. Cowie and I. D. Mackinnon, *ACS Appl. Mater. Interfaces*, 2021, **13**, 45505–45520.
62 C. Alex, S. C. Sarma, S. C. Peter and N. S. John, *ACS Appl. Mater. Interfaces*, 2020, **3**, 5439–5447.
63 Y. Wang, C. Chen and D. Zhang, *J. Mater. Chem. C*, 2021, **9**, 15445–15451.
64 Y. Piao, V. N. Tondare, C. S. Davis, J. M. Gorham, E. J. Petersen, J. W. Gilman, K. Scott, A. E. Vladár and A. R. H. Walker, *Compos. Sci. Technol.*, 2021, **208**, 108753.
65 H. Kanso, R. M. Clarke, A. Kochem, H. Arora, C. Philouze, O. Jarjayes, T. Storr and F. Thomas, *Inorg. Chem.*, 2020, **59**, 5133–5148.
66 V. S. Wadi, K. K. Jena, K. Halique and S. M. Alhassan, *ACS Appl. Polym. Mater.*, 2019, **2**, 198–208.
67 S. Zhou, Z. Ye, S. Hu, C. Hao, X. Wang, C. Huang and F. Wu, *Nanoscale*, 2018, **10**, 15771–15781.
68 S. E. Skrabalak, J. Chen, Y. Sun, X. Lu, L. Au, C. M. Cobley and Y. Xia, *Acc. Chem. Res.*, 2008, **41**, 1587–1595.
69 T. Xian, H. Li, X. Sun, Y. Huo, L. Di, C. Sun and H. Yang, *ACS Appl. Nano Mater.*, 2022, **5**, 15260–15271.
70 J. J. Bohning, *J. Chem. Educ.*, 1960, **37**, A443.
71 R. Li, Q. D. An, B. Q. Mao, Z. Y. Xiao, S. R. Zhai and Z. Shi, *J. Taiwan Inst. Chem. Eng.*, 2017, **80**, 596–606.
72 P. C. Bandara, J. Peña-Bahamonde and D. F. Rodrigues, *Sci. Rep.*, 2020, **10**, 9237.
73 Z. Wu, X. Mao, Q. Zi, R. Zhang, T. Dou and A. C. Yip, *J. Power Sources*, 2014, **268**, 596–603.
74 D. R. Lindsay, K. J. Farley and R. F. Carbonaro, *J. Environ. Monit.*, 2012, **14**, 1789–1797.
75 J. W. Ball and D. K. Nordstrom, *J. Chem. Eng. Data*, 1998, **43**, 895–918.
76 G. Sharma and B. Kandasubramanian, *J. Chem. Eng. Data*, 2020, **65**, 396–418.
77 P. S. Minhas, J. K. Saha, M. L. Dotaniya, A. Sarkar and M. Saha, *Sci. Total Environ.*, 2022, **808**, 152001.

78 K. Wang, S. Zhan, D. Zhang, H. Sun, X. Jin and J. Wang, *Colloids Surf. A: Physicochem Eng.*, 2021, **618**, 126362.
79 G. Gogoi, P. Saikia, M. J. Baruah, S. Lee, Y. B. Park, R. Dutta and K. K. Bania, *Microporous Mesoporous Mater.*, 2021, **326**, 111392.
80 A. Abdelhaleem and W. Chu, *J. Hazard. Mater.*, 2017, **338**, 491–501.
81 L. G. Devi, P. M. Nithya and R. Kavitha, *Mater. Today Commun.*, 2018, **17**, 391–401.
82 Z. Huang, S. Jia, J. Wei and Z. Shao, *RSC Adv.*, 2021, **11**, 16747–16754.
83 Y. Xiao, Y. Jiang, X. Liu, W. Zhang, Z. Zhu, Y. Gao, H. Xu, J. Zhang, Z. Liu and L. Ni, *J. Mater. Sci.*, 2020, **55**, 14211–14228.
84 W. Yan, Y. Yu, H. Zou, X. Wang, P. Li, W. Gao, J. Wang, S. Wu and K. Ding, *Solar RRL*, 2018, **2**, 1800058.
85 N. R. Chodankar, H. D. Pham, A. K. Nanjundan, J. F. Fernando, K. Jayaramulu, D. Golberg, Y. K. Han and D. P. Dubal, *Small*, 2020, **16**, 2002806.